Research Article Vol. 13, No. 2 / February 2026 / Optica 273

OPTICA

Near-perfect efficiency in X-ray phase microtomography

Dominik John,[1,2,*] Gregor Breitenhuber,[1] Sami Wirtensohn,[1,2] Franziska Hinterdobler,[1] Luka Gaetani,[1] Sara Savatović,[1,3] Jens Lucht,[4] Markus Osterhoff,[4] Marina Eckermann,[5] Tim Salditt,[4] and Julia Herzen[1]

[1]Research Group Biomedical Imaging Physics, Department of Physics, TUM School of Natural Sciences & Munich Institute of Biomedical Engineering, Technical University of Munich, James-Franck-Straße 1, 85748 Garching, Germany
[2]Helmholtz-Zentrum Hereon, Institute of Materials Physics, 21502 Geesthacht, Germany
[3]Department of Physics and Astronomy "Galileo Galilei", University of Padua, 35131 Padua, Italy
[4]Institut für Röntgenphysik, Georg-August-Universität Göttingen, Friedrich-Hund-Platz 1, 37077 Göttingen, Germany
[5]Institute of Applied Physics, Universität Bern, Sidlerstrasse 5, 3012 Bern, Switzerland
*dominik.john@tum.de

Received 10 November 2025; revised 18 December 2025; accepted 7 January 2026; published 5 February 2026

X-ray microtomography at synchrotron sources is fundamentally limited by the high radiation dose applied to the samples, which restricts investigations to non-native tissue states and thereby compromises the biological relevance of the resulting data. The limitation stems from inefficient indirect detection schemes that require prolonged exposures. Efforts to extract additional contrast through multi-modal techniques, like modulation-based imaging, worsen the problem by requiring multiple tomographic scans. In addition, the techniques suffer from low modulator pattern visibility, which reduces measurement efficiency and sensitivity. We address both the detection efficiency and modulation visibility challenges using a setup that combines an X-ray waveguide, a structured phase modulator, and a photon-counting detector. Our approach simultaneously achieves near-theoretical limits in both visibility (95%) and quantum efficiency (98%), thereby enabling dose-efficient multi-modal microtomography at single-micrometer resolution. This advance represents an important step toward routine multi-modal microtomography of native-state biological specimens with the potential to advance biomedical research and disease diagnosis.

https://doi.org/10.1364/OPTICA.584432

1. INTRODUCTION

X-ray micro-computed tomography (μCT) has enabled valuable three-dimensional insights into biological specimens [1–8] and is often considered a non-destructive imaging technique. However, recent investigations have revealed that radiation damage at synchrotron sources poses a significant challenge: intense X-ray exposure causes severe cellular damage [9], with structural changes detectable from the first moments of exposure [10]. These pitfalls limit the reliability of imaging-derived data in biological research [9]. High photon flux also produces radicals in wet specimens [11], leading to gas bubble formation and sample deformation. To prevent this, samples are typically embedded in paraffin [12] or ethanol [13], neither of which preserves the native tissue environment.

While computational approaches are being investigated to mitigate dose requirements [14], the root of the dose problem lies in the detection technology itself. High-resolution μCT setups at synchrotrons and laboratories employ CCD or CMOS chips coupled to scintillators [15], which present a fundamental trade-off between spatial resolution and efficiency: Thicker scintillators increase efficiency but introduce signal blurring. The poor quantum efficiency of these indirect detectors means that much of the radiation passing through the sample is not detected, necessitating higher doses to achieve acceptable image quality. Photon-counting (or direct) detectors circumvent this trade-off, providing dose-efficient imaging through high quantum efficiency [16,17], noise-free readout, and sharp pixel response across high dynamic ranges. These advantages have been successfully demonstrated at laboratory sources [16,18]. However, the comparatively large pixel size of at least 55 μm [19] has precluded the use of direct detectors for high-resolution synchrotron microtomography, where effective pixel sizes in the single-micrometer range are required.

The challenge of dose-efficient imaging is further complicated by the need for enhanced contrast. Many biological tissues exhibit low contrast in conventional attenuation-based imaging, necessitating the development of methods to additionally exploit the phase shift and scattering introduced by the samples. Some of these methods rely on the free-space propagation of the X-ray wavefront as a contrast mechanism and include propagation-based imaging [20–22], holography [23], and ptychography [24]. Other techniques employ additional optical elements such as crystal

analyzers [25], gratings [26,27], or various wavefront markers [28–30]. Speckle-based imaging [28,31,32], also more generally referred to as modulation-based imaging to include structured diffusers [33,34], uses wavefront markers to track changes and displacements in the X-ray wavefront imparted by a sample. This is performed either by explicitly tracking changes in subregions of the image [31,35] or using a global algorithmic approach [36,37]. One advantage of the modulation-based approach compared to optics-free methods is that it enables the simultaneous extraction of three imaging modalities related to the sample's properties: transmission, phase, and small-angle scattering (also known as dark field). In addition, the method enables a quantitative rather than qualitative access to the phase of the examined object in the form of electron density maps [38] free of prior assumptions on the sample composition [12]. However, these benefits come at the cost of acquiring multiple tomographic scans at different modulator positions, leading to increased measurement time and sample dose.

The efficiency of modulation-based imaging critically depends on achieving high visibility, which characterizes the intensity differences in the modulation pattern and directly relates to signal-to-noise ratio [39,40]. High visibility enables the analysis of weaker signals and permits shortened measurement times, making it essential for measurement and dose efficiency. To address this need, 2D Talbot array illuminators (TAIs) have been recently introduced to increase visibility [30]. Unlike random modulators, such as sandpaper, these optical elements create phase shifts in the wavefront in a regular pattern, with the shift magnitude optimized for maximum visibility at specific energies and measurement distances. While advances in the modulator provide one avenue for increasing visibility, increasing the coherence of the source provides another complementary approach. X-ray waveguides have emerged as a useful tool for creating highly coherent point sources [41]. Combined with suitable focusing optics [42,43], waveguide-based sources have, for example, been successfully applied to investigate human pathology [3,4] using propagation-based imaging.

To simultaneously overcome the mentioned dose efficiency and visibility limitations of conventional micro-computed tomography setups, we propose a novel setup that combines X-ray waveguides with Talbot array illuminators and a photon-counting detector, which has a quantum efficiency of 98% at 8 keV [44]. We experimentally characterize the setup's properties by measuring the achieved visibilities over a range of propagation distances and determine the angular sensitivity using both a direct and an indirect detector. Additionally, we demonstrate the method's multi-modal capabilities by acquiring a dark-field projection of a silicon pillar and performing a phase tomography of biological tissue.

2. RESULTS

A. Setup Design

A schematic drawing of the proposed setup is shown in Fig. 1. The main components consist of Kirkpatrick–Baez (KB) mirrors that focus the incoming X-rays onto an X-ray waveguide, which produces a small focal spot with a smooth wavefront. A Talbot array illuminator is placed a distance s downstream of the waveguide to serve as a phase modulator. The setup was tested with both photon-counting and scintillator-based detectors for comparison. More details on the components can be found in Section 4.H.

B. Visibility

We placed different phase modulators at varying distances downstream of the waveguide, keeping the detector position fixed, and recorded the resulting visibilities. The experiment was conducted at two different beam energies of 8 and 10 keV. Figure 2 shows a comparison of visibilities for different modulators for two detector types: the photon-counting detector and the CMOS detector.

Peak visibility was similar for all structured modulators and was significantly higher than that of the Kapton random diffuser. The CMOS camera achieved a maximum visibility of 94.7% and the photon-counting detector reached 93.4% for the 8 keV case using the 10 μm period modulator. As expected, given the fundamental optical properties of the setup, the performance between the two detector types was similar. A key finding is that the visibility remains stable over a large range of propagation distances, particularly for the CMOS detector. For the photon-counting detector, the visibility drops as the effective pixel size approaches the modulator period. This is expected, since the modulation pattern is no longer adequately sampled. In contrast, the effective pixel size of the CMOS detector remains small enough to adequately sample the modulation pattern across the entire measurement range.

The visual impression of the recorded modulation patterns confirms the quantitative visibility measurements. Bright intensity maxima are positioned next to regions of almost no intensity in both detector cases, demonstrating the high contrast. Figure 3(a) shows a visibility map corresponding to the intensity pattern of the photon-counting detector in Fig. 2(c). The map shows high spatial uniformity with a mean signal of 93.4% and a standard deviation of $\sigma = 2.4\%$. The visibility distribution of the CMOS detector

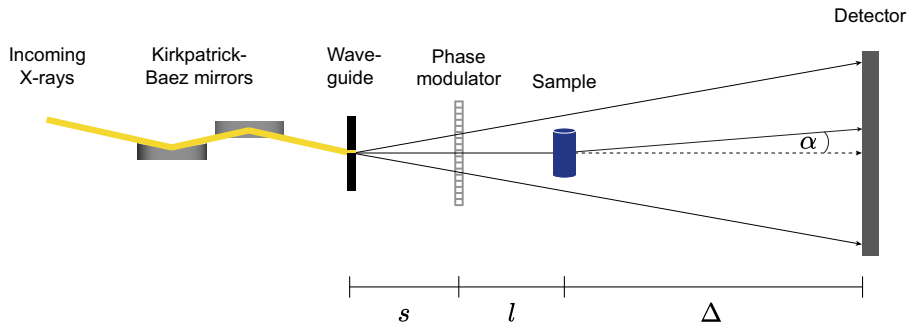

Fig. 1. The radiation produced by an undulator source and filtered by a monochromator (not shown) is focused onto a waveguide via a Kirkpatrick–Baez mirror. A phase modulator is placed a distance s downstream of the waveguide, and the sample is located a distance l downstream of the Talbot array. The detector is placed a distance Δ downstream of the sample. Due to the presence of the sample, phase effects lead to a refraction of the reference pattern by an angle α.

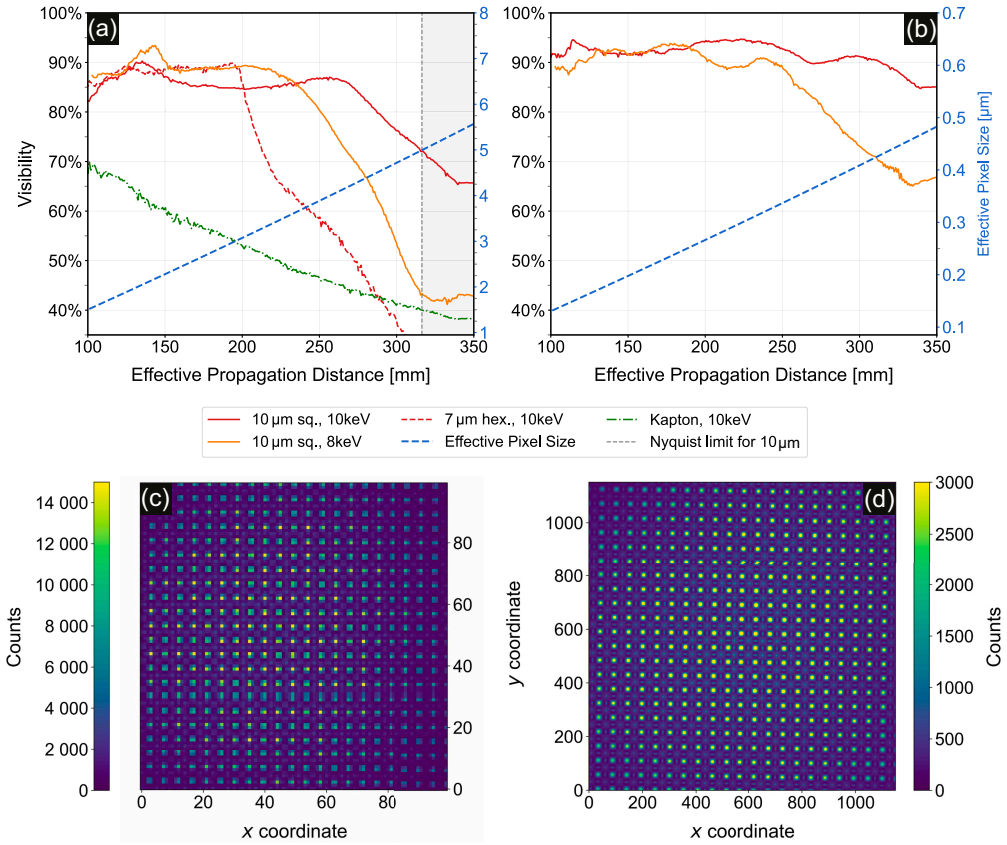

Fig. 2. Visibility versus effective propagation distance for different phase modulators. The top panels show the visibility as a function of the effective propagation distance for both detector types. The photon-counting detector camera (a) achieves a maximum visibility of 93.4%, and the CMOS detector (b) reaches 94.7%. The blue dashed line indicates how the effective pixel size increases with the propagation distance. The gray dotted line in (a) marks the Nyquist limit above which a 10 µm period modulator pattern can no longer be properly sampled. The bottom panels display the modulation patterns captured by each detector system at their respective maximum visibilities. Both use the 10 µm period TAI. The intensity pattern of the photon-counting detector (c) was captured at a beam energy of 8 keV, and the pattern of the CMOS detector (d) was imaged at a beam energy of 10 keV. The strong and regular intensity changes are clearly visible; however, the CMOS detector resolves the pattern better due to its smaller pixel size. The blur at approximately $y = 30$ in the photon-counting detector panel is due to the interpolation of the detector gap.

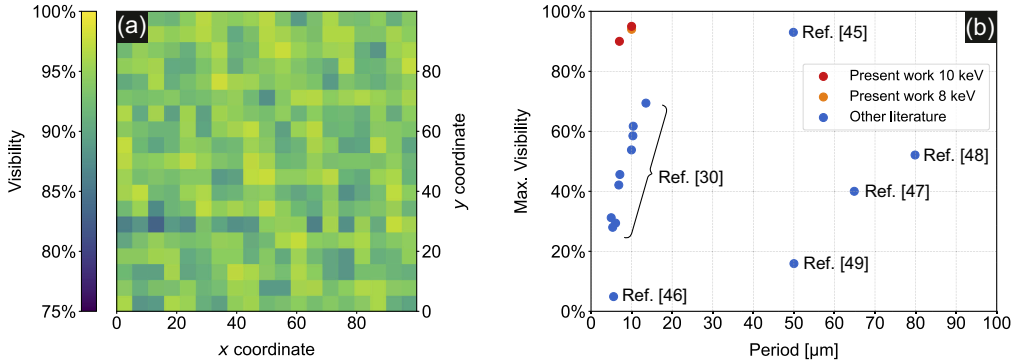

Fig. 3. (a) Visibility map corresponding to the intensity pattern in Fig. 2(c). The visibility appears very spatially uniform with a mean value of 93.4% and a standard deviation of $\sigma = 2.4\%$. A slight decrease to around 80% is observed for a few patches on the axis $y = 30$, corresponding to the detector's interpolated gap. (b) Combinations of visibility and modulator period from previous literature (blue) [30,45–49] and the current work (orange and red). The highest available value for each combination was used, regardless of the detector type. Due to the strong intensity gradients created, a combination of small period size and high visibility is preferable for modulation-based retrieval of phase shifts. Compared to previous literature, our approach enables visibility values close to the theoretical upper limit of 100% at small period sizes.

(not depicted) is similar at 94.7% with $\sigma = 0.4\%$. The comparatively lower standard deviation likely stems from the absence of an interpolation region and the smoother sampling of the intensity pattern due to the lower pixel size.

Figure 3 shows different combinations of structure period sizes and the visibility that has been achieved. For imaging applications, smaller period sizes at high visibility are preferable, since they create strong intensity gradients even at the scale of smaller

Table 1. Comparison of Angular Sensitivities (Minimum Resolvable Refraction Angle) of the Two Detector Types for Identical Measurement Conditions[a]

	Photon Counter	CMOS Camera
Eff. pix. size [μm]	3.83	3.66
σ_x [nrad]	**1.08**	1.55
σ_y [nrad]	**1.11**	1.49
$\sigma_{(x,y)}$ [nrad]	**1.55**	2.15

[a]Favorable values are marked in bold font.

sample features. Although a visibility of 93% has been reported for a period of 50 μm [45], a similar value has not yet been achieved for significantly smaller structure sizes. Our reported setup provides a visibility close to the theoretical maximum for period sizes of 10 and 7 μm. Moreover, the employed compound optics, the Kirkpatrick–Baez mirrors and the X-ray waveguide, are non-dispersive. This allows for rapid changes in energy and was utilized for the switch from 8 to 10 keV.

C. Angular Sensitivity

The phase sensitivity was determined by acquiring a projection of a test object with 26 modulator positions. The same object was imaged with an exposure time of 1.0 s and a sample distance $s = 260$ mm using both the photon-counting detector and the CMOS camera. To match the resolution of the photon-counting detector, the CMOS camera data were binned by a factor of 11 prior to phase retrieval. In both cases, the unified modulated pattern analysis (UMPA) [31,50] was used to track the local displacement of the pattern, corresponding to the refraction angles. The UMPA analyzer window was set to $w = 1$, corresponding to a 3×3 pixel analysis region. A background region containing 2520 pixels was selected above the test object in the differential phase images captured with both detectors. This region was used to calculate the standard deviation, which was then converted into an angular sensitivity, as described in Section 4.E. A comparison of angular sensitivities is provided in Table 1.

The results show that, given the same exposure time, the bidirectional angular sensitivity of the setup with the binned, fiber-coupled CMOS camera is 39% lower than that of the setup with the photon-counting detector. This indicates a less efficient use of the incoming photons. Moreover, similar values for angular sensitivity in the x and y directions confirm that the stepping protocol resulted in bidirectional phase sensitivity. Our achieved angular sensitivity of 1.55 nrad compares favorably to the previously reported value of about 143 nrad in a parallel-beam configuration. However, the smaller effective pixel size of 0.96 μm needs to be considered [30]. We additionally note that high-resolution micro-computed tomography is typically performed with magnification lenses rather than fiber-coupling to reach smaller pixel sizes [15,51], which further reduces detector efficiency.

Although the reported sensitivity in the examined background region is high, it may be negatively affected inside the sample region due to Laplacian phase effects. Since UMPA only models first-order phase effects, i.e., changes in the refraction angle due to the sample, unaccounted-for second-order effects may lead to artifacts or noise. In this first demonstration of the setup, the effective propagation distance was close to the critical value of the near-field assumption ($z_{\text{eff}}/z_c \approx 0.5$).

D. Dark-Field Projection

One of the key advantages of modulation-based imaging is its ability to simultaneously extract complementary contrast channels: attenuation, phase, and dark-field signals. To demonstrate that the multi-modal nature of the method is fully accessible in the proposed setup, we present both the transmission and dark-field projections of a silicon wedge in Fig. 4, while the (bidirectional) phase capabilities are demonstrated in projection and tomography in Section 2.E.

The examined silicon sample was mechanically machined to create a wedge geometry with decreasing thickness toward the top. The transmission image shown in Fig. 4(a) predominantly shows this thickness variation as a mostly uniform attenuation with a gradual decrease toward the thinner top section. In contrast, the dark-field channel shown in Fig. 4(b) reveals additional structural information alongside potential defects in the material introduced during fabrication. Several inhomogeneities are visible in the dark-field image (marked by blue and red arrows): features indicated by blue arrows are barely visible in transmission, while those marked in red arrows are present in both modalities but exhibit significantly stronger contrast in dark field. The inset histograms quantify the intensity distributions within the dotted rectangular regions, with red arrows marking the intensities corresponding to bright spots.

The fact that the dark-field signal stays mostly uniform over the entire region suggests that the scattering originates from the crystal

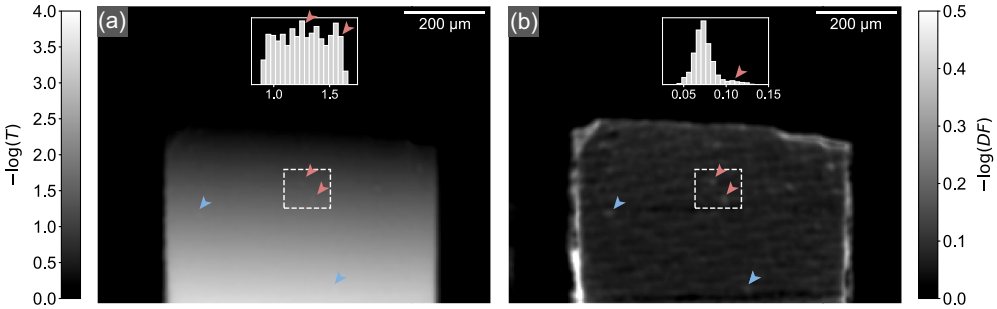

Fig. 4. Multi-modal projection images of a silicon wedge with thickness decreasing toward the top. (a) Negative logarithm of the transmission signal showing mostly uniform attenuation with a gradual decrease toward the thinner top section. (b) Negative logarithm of the dark-field signal revealing additional structural details, including inhomogeneities (blue and red arrows). All features are more prominent in the dark-field image: those marked by blue arrows are barely visible in transmission, while those marked in red arrows are present in both modalities but exhibit stronger contrast in dark field, as quantified by the inset histograms showing intensity distributions within the dotted rectangular regions. The red arrows in the histograms mark the intensities corresponding to the bright spots. The enhanced signal at the wedge edges arises from the sharp refractive-index transition between silicon and air.

surface, where the defects were likely introduced during manufacturing. If the scattering signal was to originate from the inside of the sample, it would be expected to follow a similar signal distribution as the transmission. The dark-field signal is also elevated at the sample edges due to the sharp change in electron density (or refractive index transition) from air to silicon. The complementary information provided by these contrast channels enables a more complete characterization of the material.

E. Tomographic Measurement

To demonstrate the capabilities of the combined setup for biological specimens, a piece of mouse skin embedded in a cylindrical block of paraffin wax was imaged. Two example differential phase projections are shown in Figs. 5(a) and 5(b). The differential phase signals in the x and y directions illustrate the bidirectional phase sensitivity successfully achieved with the 1D stepping approach described in Section 4.C. Figure 5(c) shows a slice through the reconstructed electron density volume. In the reconstruction, the different skin layers are well discernible against the paraffin. The 3D rendering in Fig. 5(d) shows the extent and position of the hairs—reported in the literature to have diameters on the order of 18 µm [52]—which can be well traced along their paths. Similar to the approach in Ref. [12], the spatial resolution was estimated by examining 30 line profiles across edges (in this case, across hairs) in multiple axial slices to calculate the full width at half-maximum (FWHM), resulting in a value of (9.4 ± 1.7) µm. The electron density value of subcutaneous adipose tissue agrees well with previously reported literature values for white fat in the range of 306−312 nm^{-3} [53], demonstrating the quantitative accuracy of the method. Following the calculations outlined in Section 4.G, we obtain an estimated sample dose of 1.1 kGy for the full multi-modal tomography.

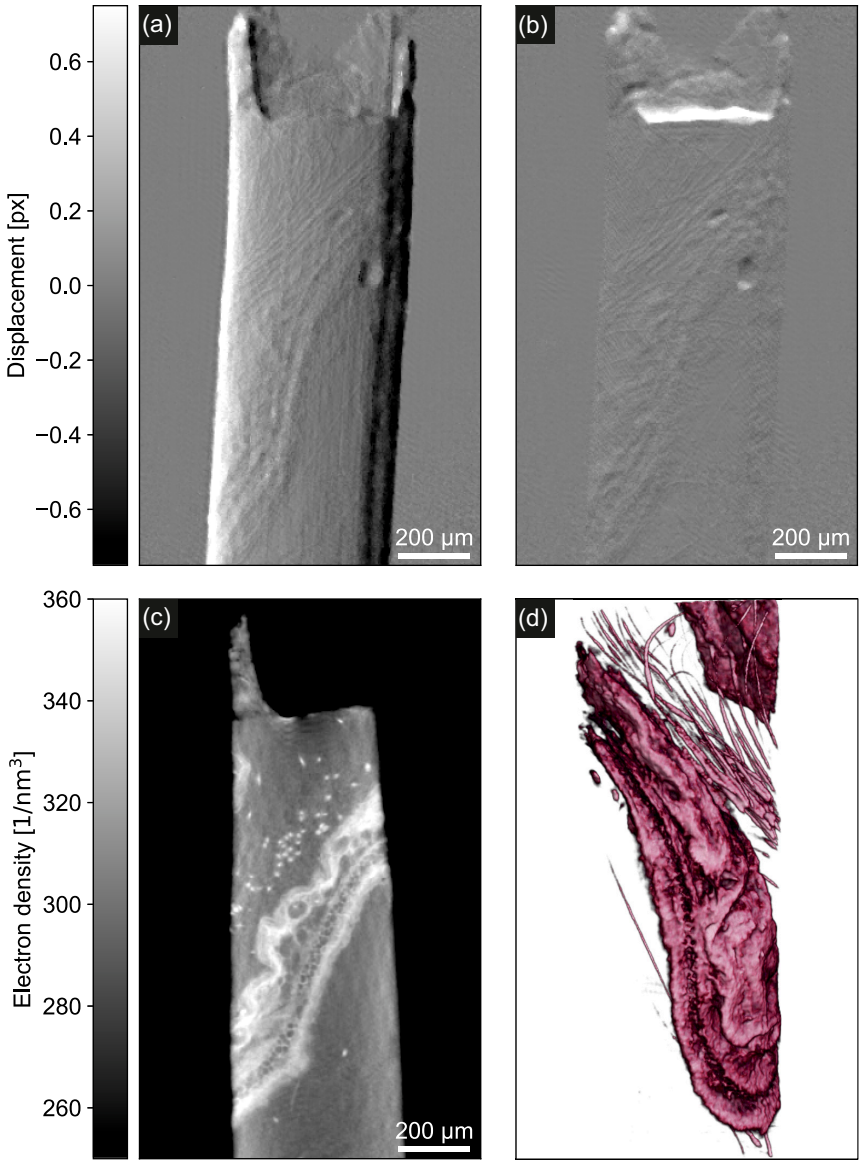

Fig. 5. Tomographic phase scan of mouse skin embedded in a cylindrical piece of paraffin. (a) and (b) show projections of the differential phase signal projections in x and y directions, respectively. These signals track the displacement of the reference pattern by the sample, in pixels, at the detector face. (c) shows a slice through the middle of the three-dimensional electron density map, obtained by 2D Fourier integration of differential signals and tomographic reconstruction. (d) is a 3D rendering of the electron density volume.

3. DISCUSSION

In this work, we have provided the first demonstration of modulation-based imaging in conjunction with X-ray waveguides, achieving visibility values of 94.7% for the CMOS and 93.4% for the photon-counting detector. This performance approaches the theoretical maximum of 100%, despite using modulators with small periods of at most 10 µm. Our measurements reveal that high visibility is maintained over a broad range of effective propagation distances (approx. 100–300 mm), which has useful practical implications for experimental flexibility.

The waveguide's magnification properties enable compatibility with large-pixel, photon-counting detectors while maintaining a spatial resolution similar to that of parallel-beam microtomography with conventional, indirect detectors. The combination of near-optimal quantum efficiency and high visibility directly addresses the dose problem in multi-modal microtomography, opening new possibilities for quantitative, multi-modal scans of samples. For the multi-modal tomography, a dose of 1.1 kGy was achieved. This is, for example, far below the limit of 35 kGy reported for degradation in the mechanical properties of cortical bone [54] and would allow multiple full tomographic scans without negatively impacting the bone's integrity. The achieved dose of 1.1 kGy is also only marginally above the 1 kGy threshold at which effects on the life span of the model organism *C. elegans* begin to emerge [55]. Future studies on biological samples could therefore use this approach to retrieve multi-modal tomograms in the most efficient manner.

As demonstrated, incorporating phase modulators also provides access to the dark-field signal, which has not yet been explored in conjunction with X-ray waveguides. We have provided a dark-field projection of a silicon crystal, showing the signal's benefits for revealing sample substructures. The signal was not included in our analysis of the mouse skin, as no significant dark field is expected from this soft tissue sample. Future tomographic experiments should therefore examine biological samples with small-angle scattering-inducing microstructure, either also using an UMPA [31] or a single-grid dark-field method for signal retrieval [56,57]. In principle, the dark-field signal provides a particularly dose-efficient means of characterizing sub-resolution features, as it yields information about microstructure below the spatial resolution limit without requiring direct resolution of these features. This approach is beneficial because directly resolving such features would require significantly higher doses due to the fourth-order relationship between applied dose and achieved resolution [58]. This capability, combined with the simultaneous acquisition of transmission and phase contrast, enables comprehensive characterization of heterogeneous samples at micrometer resolution with applications such as material decomposition [59]. While methods such as ptychography or holotomography can achieve much higher spatial resolutions (10s of nanometers or below) [24], they operate at inherently higher radiation doses and lack the dark-field channel, making the approach presented here better suited for dose-sensitive biological samples requiring multi-contrast characterization.

Despite the demonstrated potential, several aspects of the method require further optimization for high-throughput applications. First, the flux reduction introduced by the waveguide should be mitigated by improving the coupling efficiency with the KB mirror. In this experiment, the ratio of waveguide area A_{WG} to focus size A_{KB} was approximately $\eta = 16\%$. Combined with the synchrotron operating in a low-current mode with widely-spaced electron bunches at the time of measurement, this resulted in a relatively long total exposure time of approximately 2 h for the tomographic scan. However, focus sizes at or below 100 nm have been previously reported in the literature for KB mirrors [60,61], some even reaching into the sub-5 nm regime when combined with a multilayer Laue lens [62]. Next-generation synchrotron sources with their enhanced brilliance will also naturally address this limitation.

Second, temporal efficiency can be improved by optimizing the data acquisition strategy. The number of phase steps used in this work (26 steps) was chosen conservatively while establishing this new measurement methodology, but typical values reported in the literature are 9, 16, or 20 phase steps [12,30,34]. The impact of reducing phase steps could not be assessed retrospectively from the acquired data, as the employed 1D stepping scheme requires the full amount of steps to adequately sample the intensity pattern (see Section 4.C). However, it is likely that the additional phase steps provide diminishing returns, which should be investigated in future work to determine how much the number of steps can be reduced without significantly compromising reconstruction quality. For this purpose, a 2-linear-stage-based sampling scheme would be preferable over the 1D stepping method employed here, as it would allow more systematic exploration of the phase-stepping parameter space. Additionally, the tomographic scan reported here was conducted in a step-and-shoot manner, leading to significant motor overhead of 3.5 h. The overhead could be mostly eliminated using established fly-scan methods with continuous sample rotation, which are the routine method for modulation-based tomography [12,30,34].

Third, regarding the spatial coverage of the method: in the waveguide-based approach, the field of view naturally scales with the measurement geometry and the opening angle of the waveguide's exit cone, rather than being constrained by the initial beam size from the source. While the vertical field of view of the setup in this work (∼1.2 mm) is comparable to that of some parallel-beam µCT setups (e.g., Imaging Beamline P05 at PETRA III and Berkeley ALS beamline 8.3.2, both with 2 mm [63,64]), the horizontal field of view (also ∼1.2 mm) is smaller than typically achieved at such setups. Parallel-beam µCT systems usually feature horizontal beam widths of 5 mm or larger for high-resolution applications [63–65].

To make the proposed method more useful for larger biological samples, the field of view will therefore need to be expanded. One option is to manufacture and use waveguides with larger opening angles, as the achievable field of view is directly proportional to the opening angle for otherwise unchanged measurement parameters. Another option is to increase both the waveguide-sample and sample-detector distances, which was not possible in this experiment due to a space constraint of approximately 5 m for the waveguide-detector distance.

Beyond hardware modifications, several scanning approaches can extend the field of view: performing scans with an offset rotation axis [59], using stitching approaches [13], or retrieving extended projections from multiple sample positions using a modified version of the UMPA model [66]. These methods also address time-varying modulator position changes, either by incorporating drift into the UMPA model [66,67] or by maintaining sample-free regions to track it [13,59]. Region-of-interest (ROI) scans remain challenging: the sample-free approach requires empty

space in every projection, while with the UMPA-based correction an ROI scan is possible given a calibration material (e.g., air, plastic, and wax) for quantitative retrieval of electron densities (see Section 4.D).

It is worth noting, however, that with the ongoing upgrades to fourth-generation synchrotron sources, the trend in full-field imaging is moving toward smaller fields of view, as exemplified by the ForMAX beamline at MAX IV with typical beam sizes of $\sim 0.8 - 1.5$ mm [68]. In such cases, the waveguide approach would provide a clear benefit in increasing the achievable field of view.

Finally, the phase retrieval artifacts, which are likely caused by second-order phase effects, should be addressed by adapting the retrieval model to properly account for all wavefront changes induced by the sample. Another option may be to introduce a decoherer in the form of a spinning diffusor to reduce these effects [69].

In summary, our results demonstrate that combining waveguide sources, Talbot array illuminators, and photon-counting detectors enables the simultaneous achievement of high spatial resolution and optimal dose efficiency in multi-modal X-ray imaging. The method's compatibility with photon-counting detectors, high visibility, and flexible working distance makes it particularly well suited for quantitative imaging of radiation-sensitive biological samples. While several aspects require further optimization for routine high-throughput use, the fundamental capabilities demonstrated here establish a promising platform for leveraging current and fourth-generation synchrotron sources in biomedical and materials science applications.

4. MATERIALS AND METHODS

A. Theoretical Considerations

To utilize modulation-based imaging in conjunction with a waveguide focusing optic and a large-pixel photon-counting detector, several constraints must be considered. Since the algorithms tracking the sample-induced distortions of the phase modulator typically assume the X-ray near-field regime, the effective propagation distance may not become too large. A useful criterion for validating the near-field assumption is the critical propagation distance:

$$z_c = \frac{(2p_{\text{eff}})^2}{\lambda}, \tag{1}$$

where $p_{\text{eff}} = p/M$ is the effective detector pixel size (given the physical pixel size p and the optical magnification M), and λ is the X-ray wavelength [70]. The propagation distance in the experiment shall be kept well below this value to minimize the presence of higher-order phase effects that are not accounted for in modulator-tracking algorithms.

Since the proposed setup makes use of a cone-beam geometry, the physical propagation distance between the sample and the detector z needs to be replaced by an effective propagation distance z_{eff}. This follows from the Fresnel scaling theorem, which states that under the Fresnel approximation, an X-ray intensity field I in a cone-beam geometry is related to an intensity field $I^{(P)}$ in a parallel-beam scenario via

$$I(x, y, z = \Delta) = \frac{1}{M^2} I^{(P)}\left(\frac{x}{M}, \frac{y}{M}, z = \frac{\Delta}{M}\right). \tag{2}$$

Here, (x, y) are the transverse coordinates and $z = \Delta$ is the propagation distance [71]. The relevant quantity for calculating whether the setup is below the critical propagation distance is thus the effective propagation distance:

$$z_{\text{eff}} = \frac{\Delta}{M}. \tag{3}$$

As an additional constraint, the magnification must be large enough to compensate for the larger pixel size of photon-counting detectors and enable imaging applications with effective pixel sizes in the common range for synchrotron-based μCT, i.e., 1–5 μm. In summary, the constraints on the setup are (i) keeping the effective propagation distance below the critical value to stay in the near field and (ii) magnifying the sample enough to compensate for the larger pixel size of photon-counting detectors. In addition, (iii) optics with the highest possible opening angle should be used to enable larger fields of view. Theoretically, (iv) the chosen propagation distance should also coincide with a (fractional) Talbot distance d_T of the phase modulator to maximize visibility, though it has been shown experimentally in Fig. 2 that this condition may be dropped.

B. Visibility Analysis

Different approaches exist for calculating the visibility of a phase modulator [32]. In this work, we make use of the visibility definition

$$V = \frac{I_{\max} - I_{\min}}{I_{\max} + I_{\min}}, \tag{4}$$

where $I_{\max}$ is the maximum and $I_{\min}$ is the minimum recorded intensity in a subregion of the image, as previously used for structured modulators in Ref. [30]. We analyze the patch-wise visibility by subdividing the image into square regions whose area is large enough to capture a full modulator period. Since the effective pixel size changes in this geometry depending on the propagation distance, we use a patch size of 5×5 pixels for all measurements. This creates an analysis window large enough to capture at least one full modulator period at all examined effective pixel sizes.

We note here that visibility is purely a property of the intensity pattern measured at the detector and is thus independent of the specific phase stepping scheme used (see Section 4.C) to sample the pattern. To achieve the best possible angular sensitivity, the visibility should therefore always be as high as possible [see Eq. (11) in Section 4.E].

C. Phase Stepping

For phase stepping, the modulator needs to be moved into different lateral positions. Bidirectional phase sensitivity requires that the intensity maxima created by the modulator are homogeneously distributed over the pixel matrix over the course of the phase stepping [30]. We make use of the unit cell sampling method discussed in Supplement 1 of Ref. [30], which involves stepping the modulator in a diagonal fashion.

The tilt angle of this diagonal and the number of phase steps are calculated as follows [30]: define two orthogonal vectors $(\mathbf{a}, \mathbf{b})$ in the modulator plane and choose their lengths in such a way that a and b are co-prime. The modulator is then moved along an axis oriented at an angle

$$\alpha = \arctan(a/b) \tag{5}$$

to one direction of the grid pattern. When a number of $N = a^2 + b^2$ phase steps is performed, no redundant sampling occurs. The size of each individual phase step is defined by d/N, d being the period of the modulator.

D. Phase Retrieval

We employ the unified modulated pattern analysis (UMPA) algorithm to track sub-pixel displacements (u_x, u_y) of the reference pattern caused by phase effects in the projection space [31]. These local displacements of the pattern, which correspond to the refraction angles (α_x, α_y), are converted from pixels on the detector face to a differential phase using

$$\left(\frac{\partial\phi}{\partial x}, \frac{\partial\phi}{\partial y}\right) = \frac{2\pi}{\lambda}(\alpha_x, \alpha_y) = (u_x, u_y)\frac{2\pi}{\lambda}\frac{p_{\text{eff}}}{z_{\text{eff}}}, \tag{6}$$

where $(\frac{\partial\phi}{\partial x}, \frac{\partial\phi}{\partial y})$ represent the x and y derivatives of the object's phase $\phi(x, y)$, λ is the wavelength, and p_{eff} is the effective pixel size [31]. We then obtain the object's phase (up to an additive constant C) through 2D Fourier integration of the two differential phase signals [72,73]:

$$\phi(x, y) = \mathcal{F}^{-1}\left(\frac{\mathcal{F}\left(\frac{\partial\phi}{\partial x} + i\frac{\partial\phi}{\partial y}\right)}{ik_x - k_y}\right) + C. \tag{7}$$

Here, $\mathcal{F}$ denotes the Fourier transformation with respect to x and y, while $\mathcal{F}^{-1}$ is the corresponding inverse Fourier transformation; (k_x, k_y) are the Fourier-space coordinates associated with (x, y). After defining the sample-free regions as having $\phi = 0$, the projected electron density is recovered using the relation:

$$\rho_{e,\perp}(x, y) = \frac{-\phi(x, y)}{\lambda\, r_e}, \tag{8}$$

where r_e is the classical electron radius [74]. In a last step, the electron density distribution of the volume is obtained through tomographic reconstruction of the acquired projections. For reconstruction, we use the *Core Imaging Library* [75,76] with the *ASTRA toolbox* [77] backend. To account for potential systematic measurement errors in UMPA, we calibrate the resulting electron density using the procedure described in Ref. [78]. We employ paraffin wax as a reference material to rescale the final electron density volume according to

$$\rho_{e,\text{cal}}(x, y, z) = \frac{\rho_{e,\text{raw}}(x, y, z) - \bar{\rho}_{e,\text{bg}}}{\bar{\rho}_{e,\text{ref}} - \bar{\rho}_{e,\text{bg}}}\,\rho_{e,\text{theo}}, \tag{9}$$

where $\rho_{e,\text{cal}}(x, y, z)$ represents the calibrated three-dimensional electron density map, $\rho_{e,\text{raw}}(x, y, z)$ is the uncalibrated electron density map, $\bar{\rho}_{e,\text{bg}}$ and $\bar{\rho}_{e,\text{ref}}$ are the mean electron densities of the background and reference material, respectively, and $\rho_{e,\text{theo}}$ is the theoretical electron density of the reference material. Using a measurement at the P05 beamline calibrated with poly(methyl methacrylate) as the reference material, the electron density of paraffin (Paraplast Plus) was determined to be $(299 \pm 7)\ \text{nm}^{-3}$.

E. Angular Sensitivity

The angular sensitivity of an X-ray imaging system is defined as the minimum detectable refraction angle α and is a widely used measure to compare different imaging systems [79]. Considering Eq. (6), it follows that

$$(\sigma_x, \sigma_y) = \sqrt{\text{Var}_{\text{BG}}\{(u_x, u_y)\}}\,\frac{p_{\text{eff}}}{z_{\text{eff}}}, \tag{10}$$

where Var_{BG} is the variance in a homogeneous region, typically the background without any sample in the beam [30, Supplement 1]. Furthermore, the angular sensitivity is linked to other imaging quantities, such as visibility and the average number of counts, N. This relationship can be described by

$$\sigma_{x/y} \propto \frac{1}{w v\sqrt{N}}, \tag{11}$$

where v is the visibility, and w is the analyzer window size used by UMPA [31,80].

F. Corrections for Beam Stability

Due to the strong intensity gradients induced by the modulators, even slight movements result in substantial changes in the recorded counts for each pixel. This is problematic because the phase-retrieval algorithm assumes that the beam profile is stable and all changes are related to sample properties [32].

To account for the movement, we decompose a number of consecutively recorded flat fields at each stepping position into eigenflats E_i using the principal component analysis, as described in Ref. [81]. Then, for each recorded projection image, we add the eigenflats using a weighted sum to best match the beam condition at the time of acquisition. This generates so-called dynamic flat-field images. The weights w_i for this sum are obtained by comparing the weighted sum to a sample-free region I_{BG} in each projection [12]:

$$w_i = \underset{w_i}{\text{argmin}} \left\| I_{\text{BG}} - \sum_i w_i\, E_i \right\|_2^2. \tag{12}$$

The method relies on the assumption that the principal components adequately capture the beam variations present during sample acquisition. The correction may perform poorly if the beam exhibits drift modes not represented in the flat-field acquisition phase. Additionally, the approach requires sufficiently large sample-free regions for reliable weight estimation, typically on the order of 10% of the field of view [12].

In comparison to using a time-averaged flat field without this correction, the mean squared error (MSE) in the sample-free region was reduced by $(77 \pm 13)\%$ across all phase steps using matched reference images. Because a residual modulator pattern was still observed in the processed projections, the peaks corresponding to the modulator frequency in the Fourier space were masked and set to zero for the dark-field projection and prior to reconstructing the tomographic scan, thereby reducing these artifacts. However, this last step was not performed for the projections used for angular sensitivity calculations.

G. Dose Estimate

Since the photon-counting detector is close to 100% efficient at the used energies and each count in the tomographic experiment corresponds to the absorbance of a photon with a well-defined energy of 10 keV, a dose estimate for the measurement is readily

Table 2. Radiation Dose for Different Acquisition Schemes

Acquisition Scheme	Total Energy	Sample Dose
Single projection	40 nJ	0.17 Gy
Full multi-modal projection	1.0 µJ	4.5 Gy
Full multi-modal tomography	0.26 mJ	1.1 kGy

obtainable. For this purpose, we first determine the mean transmission through the sample ($\bar{T} = 89\%$) as well as the total photon count in the reference image, restricted to the region covered by the sample ($N = 2.3 \times 10^8$). Since the photo effect is the dominating X-ray interaction with matter in this energy range, we assume the sample absorbs approximately 11% of the photons present in the reference image. We further make the simplifying assumption that the sample is a cylinder with a radius of $r = 0.25$ mm and a height of 1.3 mm. While the biological tissue itself likely has a density closer to water, we assume the whole cylinder has the lower density of the surrounding paraffin (0.90 g cm^{-3}). Since this results in a lower sample mass m, it yields a higher and therefore more conservative estimate of the absorbed dose $D = E/m$ for a given absorbed energy E.

In Table 2, we provide the resulting total energies and sample doses for different scenarios: a single projection at one modulator position, a full multi-modal projection (which in our case, corresponds to 26 single projections due to the sampling scheme used), and full multi-modal tomography consisting of 250 multi-modal projections.

H. Experimental Setup

The experiment was conducted at the GINIX setup [62,82,83] of the Coherence Beamline P10 (*PETRA III*, DESY, Hamburg), which uses a U32 undulator as its X-ray source. The setup is depicted in Fig. 1: after passing through a monochromator, the X-rays hit two total reflection mirrors arranged in a Kirkpatrick–Baez (KB) geometry within a vacuum vessel. The KB mirror provides a two-dimensional hard X-ray focus down to 250×250 nm^2, which is used to focus the beam onto an X-ray waveguide. This creates a highly coherent source for the experiment. We used a waveguide channel with a width and depth of $d = 100$ nm and an optical depth of $L = 1$ mm, defined by e-beam lithography in silicon (*Eulitha GmbH*, Würenlos, Switzerland) and then capped by wafer bonding. The exit flux depends on storage ring operation, photon energy, beamline settings, and alignment. For the given experiment, it reached 1.5×10^9 s^{-1}.

A holder mounted to three orthogonal linear stages was positioned at a distance s downstream of the waveguide. This allowed for the insertion of different phase modulators and precise positioning both parallel to and perpendicular to the beam direction. The sample was placed on a rotation stage at a further distance l downstream of the modulator. Two detector systems were used to acquire images: the first was an Andor Zyla sCMOS camera (*Oxford Instruments*, Tubney Woods, England) with a 15 µm thick Gadox scintillator and magnifying optics. This resulted in an effective pixel size of 6.5 µm for the array of 2160×2560 pixels. The second system used was an Eiger X4M photon-counting detector (*DECTRIS AG*, Baden, Switzerland) with 2070×2167 pixels and a pitch of 75 µm. The phase modulators used were Talbot array illuminators fabricated from silicon, as described in Ref. [30]. Due to their design height, they impart a $2\pi/3$ phase-shift to portions of the wavefront at an energy of 10 keV. Two modulators with period sizes of 7 and 10 µm were employed. The first modulator creates a hexagonal lattice of foci, while the second creates a square lattice. For comparison, a piece of Kapton B black was also used as a random diffuser.

For the tomography experiment, a mouse skin sample was placed at a distance $s = 260$ nm from the waveguide and imaged with the photon-counting detector. The beam energy was set to 10 keV, and 250 different angles were captured over 360°, each with an exposure time of 1.0 s. The projection count corresponded to approximately 1.1× the Nyquist sampling criterion for a sample with a radius of approximately 70 pixels or 270 µm. After each full rotation of the sample, the modulator was moved to its next stepping position. A total of 50 reference images were acquired at each position. For this experiment, the modulator with a period of 10 µm and a square lattice pattern was used. To achieve bidirectional phase sensitivity with 1D linear phase stepping, the modulator was stepped along an axis inclined at an angle of 11.3° to the modulator pattern. This follows from selecting the two co-prime numbers $a = 1$ and $b = 5$, resulting in a total of $5^2 + 1^2 = 26$ modulator positions, as described in Section 4.C. Phase retrieval was performed using a runtime-optimized version of UMPA [50] with a window parameter of $w = 1$, corresponding to a window size of 3×3 pixels. A projection to test phase sensitivity was acquired with the same modulator and settings, with the only differences being the number of reference images (10 instead of 50) and the sample, a silicon crystal with varying thicknesses. This same sample was imaged for the experiment in Section 2.D. Here, a window parameter of $w = 4$ was used for a robust retrieval of the dark-field signal [84], which is typically more prone to noise.

Funding. HORIZON EUROPE European Research Council (DEPICT; Julia Herzen; 101125761); HORIZON EUROPE European Innovation Council (1MICRON, 101186826); Bundesministerium für Bildung und Forschung (05K25MG2); Friedrich Naumann Stiftung.

Acknowledgment. We thank Benedikt Günther, Stefan Schwaiger, James Pollock, Jannis Ahlers, and Marie-Christine Zdora for fruitful discussions. We acknowledge DESY (Hamburg, Germany), a member of the Helmholtz Association HGF, for the provision of experimental facilities under beamtime proposal I-20241169. This research was supported in part through the Maxwell computational resources operated at DESY. The authors gratefully acknowledge financial support by the ERC Consolidator Grant (Julia Herzen, TUM, DEPICT, PE3, 101125761) and by the EIC Pathfinder (1MICRON, 101186826). The authors also acknowledge funding through the BMFTR joint project 05K25MG2, HoTop4: Optiken für die Ganzfeld-Bildgebung bei PETRA III und IV. D. John acknowledges a doctoral scholarship by the Friedrich Naumann Foundation for Freedom funded by the Bundesministerium für Forschung, Technologie und Raumfahrt (BMFTR). The authors thank Mirjam Schenk for providing the mouse skin sample.

Disclosures. The authors declare no conflicts of interest.

Data availability. Data underlying the results presented in this paper are not publicly available at this time but may be obtained from the authors upon reasonable request.

REFERENCES

1. J. Thiesse, E. Namati, J. C. Sieren, *et al.*, "Lung structure phenotype variation in inbred mouse strains revealed through in vivo micro-CT imaging," J. Appl. Physiol. **109**, 1960–1968 (2010).
2. S. J. Schambach, S. Bag, L. Schilling, *et al.*, "Application of micro-CT in small animal imaging," Methods **50**, 2–13 (2010).
3. M. Eckermann, J. Frohn, M. Reichardt, *et al.*, "3D virtual pathohistology of lung tissue from Covid-19 patients based on phase contrast X-ray tomography," eLife **9**, e60408 (2020).

4. M. Reichardt, P. M. Jensen, V. A. Dahl, *et al.*, "3D virtual histopathology of cardiac tissue from Covid-19 patients based on phase-contrast X-ray tomography," eLife **10**, e71359 (2021).
5. A. Shakeri-Zadeh, "How can molecular micro-CT imaging revolutionize drug discovery?" Expert Opin. Drug Discov. **14**, 849–853 (2019).
6. B. D. Metscher, "MicroCT for developmental biology: a versatile tool for high-contrast 3D imaging at histological resolutions," Dev. Dyn. **238**, 632–640 (2009).
7. B. D. Metscher, "MicroCT for comparative morphology: simple staining methods allow high-contrast 3D imaging of diverse non-mineralized animal tissues," BMC Physiol. **9**, 11 (2009).
8. F. Friedrich and R. G. Beutel, "Micro-computer tomography and a renaissance of insect morphology," Proc. SPIE **7078**, 545–550 (2008).
9. F. Petruzzellis, C. Pagliarani, T. Savi, *et al.*, "The pitfalls of in vivo imaging techniques: evidence for cellular damage caused by synchrotron X-ray computed micro-tomography," New Phytol. **220**, 104–110 (2018).
10. K. Sauer, I. Zizak, J.-B. Forien, *et al.*, "Primary radiation damage in bone evolves via collagen destruction by photoelectrons and secondary emission self-absorption," Nat. Commun. **13**, 7829 (2022).
11. E. F. Fornasiero and S. O. Rizzoli, *Super-Resolution Microscopy Techniques in the Neurosciences* (Springer, 2014).
12. M. Riedel, K. Taphorn, A. Gustschin, *et al.*, "Comparing X-ray phase-contrast imaging using a Talbot array illuminator to propagation-based imaging for non-homogeneous biomedical samples," Sci. Rep. **13**, 6996 (2023).
13. D. John, J. Chen, C. Gaßner, *et al.*, "Centimeter-sized objects at micrometer resolution: extending field-of-view in wavefront marker X-ray phase-contrast tomography," arXiv (2024).
14. Y. Obata, D. Y. Parkinson, D. M. Pelt, *et al.*, "Enhancing synchrotron radiation micro-CT images using deep learning: an application of Noise2Inverse on bone imaging," Synchrotron Radiat **32**, 690–699 (2025).
15. E. Longo, A. Contillo, L. D'Amico, *et al.*, "SYRMEP beamline: state of the art, upgrades and future prospects," Eur. Phys. J. Plus **139**, 880 (2024).
16. T. Sellerer, S. Ehn, K. Mechlem, *et al.*, "Quantitative dual-energy micro-CT with a photon-counting detector for material science and non-destructive testing," PLoS One **14**, e0219659 (2019).
17. S. Gkoumas, T. Thuering, A. G. Taboada, *et al.*, "Dose-independent near-ideal DQE of a 75 m pixel GaAs photon counting spectral detector for breast imaging," Proc. SPIE **10948**, 207–213 (2019).
18. J. Scholz, L. Birnbacher, C. Petrich, *et al.*, "Biomedical X-ray imaging with a GaAs photon-counting detector: a comparative study," APL Photonics **5**, 106108 (2020).
19. D. Pennicard, S. Smoljanin, F. Pithan, *et al.*, "LAMBDA 2M GaAs—a multi-megapixel hard X-ray detector for synchrotrons," J. Instrum. **13**, C01026 (2018).
20. A. Snigirev, I. Snigireva, V. Kohn, *et al.*, "On the possibilities of X-ray phase contrast microimaging by coherent high-energy synchrotron radiation," Rev. Sci. Instrum. **66**, 5486–5492 (1995).
21. P. Cloetens, R. Barrett, J. Baruchel, *et al.*, "Phase objects in synchrotron radiation hard X-ray imaging," J. Phys. D: Appl. Phys. **29**, 133–146 (1996).
22. D. M. Paganin, S. C. Mayo, T. E. Gureyev, *et al.*, "Simultaneous phase and amplitude extraction from a single defocused image of a homogeneous object," J. Microsc. **206**, 33–40 (2002).
23. P. Cloetens, W. Ludwig, J. Baruchel, *et al.*, "Holotomography: quantitative phase tomography with micrometer resolution using hard synchrotron radiation X rays," Appl. Phys. Lett. **75**, 2912–2914 (1999).
24. F. Pfeiffer, "X-ray ptychography," Nat. Photonics **12**, 9–17 (2018).
25. A. Bravin, "Exploiting the X-ray refraction contrast with an analyser: the state of the art," J. Phys. D: Appl. Phys. **36**, A24 (2003).
26. T. Weitkamp, A. Diaz, C. David, *et al.*, "X-ray phase imaging with a grating interferometer," Opt. Express **13**, 6296–6304 (2005).
27. E. E. Bennett, R. Kopace, A. F. Stein, *et al.*, "A grating-based single-shot X-ray phase contrast and diffraction method for in vivo imaging," Med. Phys. **37**, 6047–6054 (2010).
28. K. S. Morgan, D. M. Paganin, and K. K. W. Siu, "X-ray phase imaging with a paper analyzer," Appl. Phys. Lett. **100**, 124102 (2012).
29. S. Bérujon, E. Ziegler, R. Cerbino, *et al.*, "Two-dimensional X-ray beam phase sensing," Phys. Rev. Lett. **108**, 158102 (2012).
30. A. Gustschin, M. Riedel, K. Taphorn, *et al.*, "High-resolution and sensitivity bi-directional X-ray phase contrast imaging using 2D Talbot array illuminators," Optica **8**, 1588–1595 (2021).
31. M.-C. Zdora, P. Thibault, T. Zhou, *et al.*, "X-ray phase-contrast imaging and metrology through unified modulated pattern analysis," Phys. Rev. Lett. **118**, 203903 (2017).
32. M.-C. Zdora, "State of the art of X-ray speckle-based phase-contrast and dark-field imaging," J. Imaging **4**, 60 (2018).
33. L. Quénot, S. Bohic, and E. Brun, "X-ray phase contrast imaging from synchrotron to conventional sources: a review of the existing techniques for biological applications," Appl. Sci. **12**, 9539 (2022).
34. S. Savatović, D. Laundon, F. De, *et al.*, "High-resolution X-ray phase-contrast tomography of human placenta with different wavefront markers," Sci. Rep. **15**, 2131 (2025).
35. S. Berujon and E. Ziegler, "X-ray multimodal tomography using speckle-vector tracking," Phys. Rev. Appl. **5**, 044014 (2016).
36. L. Quénot, H. Rougé-Labriet, S. Bohic, *et al.*, "Implicit tracking approach for X-ray phase-contrast imaging with a random mask and a conventional system," Optica **8**, 1412–1415 (2021).
37. S. J. Alloo, K. S. Morgan, D. M. Paganin, *et al.*, "Multimodal intrinsic speckle-tracking (MIST) to extract images of rapidly-varying diffuse X-ray dark-field," Sci. Rep. **13**, 5424 (2023).
38. M.-C. Zdora, P. Thibault, W. Kuo, *et al.*, "X-ray phase tomography with near-field speckles for three-dimensional virtual histology," Optica **7**, 1221–1227 (2020).
39. A. Yan, X. Wu, and H. Liu, "Predicting fringe visibility in dual-phase grating interferometry with polychromatic x-ray sources," J. X-Ray Sci. Technol. **28**, 1055–1067 (2020).
40. T. Neuwirth, A. Backs, A. Gustschin, *et al.*, "A high visibility talbot-lau neutron grating interferometer to investigate stress-induced magnetic degradation in electrical steel," Sci. Rep. **10**, 1764 (2020).
41. F. Pfeiffer, C. David, M. Burghammer, *et al.*, "Two-dimensional X-ray waveguides and point sources," Science **297**, 230–234 (2002).
42. A. Jarre, C. Fuhse, C. Ollinger, *et al.*, "Two-dimensional hard X-ray beam compression by combined focusing and waveguide optics," Phys. Rev. Lett. **94**, 074801 (2005).
43. T. Salditt, M. Osterhoff, M. Krenkel, *et al.*, "Compound focusing mirror and X-ray waveguide optics for coherent imaging and nano-diffraction," Synchrotron Radiat. **22**, 867–878 (2015).
44. DECTRIS Ltd., Baden, Switzerland, "Technical Specifications EIGER X 4M Detector Systems," Document Version v1.3.8 (2019).
45. T. dos Santos Rolo, S. Reich, D. Karpov, *et al.*, "A Shack-Hartmann sensor for single-shot multi-contrast imaging with hard X-rays," Appl. Sci. **8**, 737 (2018).
46. K. S. Morgan, P. Modregger, S. C. Irvine, *et al.*, "A sensitive X-ray phase contrast technique for rapid imaging using a single phase grid analyzer," Opt. Lett. **38**, 4605–4608 (2013).
47. S. Reich, T. dos Santos Rolo, A. Letzel, *et al.*, "Scalable, large area compound array refractive lens for hard X-rays," Appl. Phys. Lett. **112**, 151903 (2018).
48. M. Kagias, Z. Wang, M. E. Birkbak, *et al.*, "Diffractive small angle X-ray scattering imaging for anisotropic structures," Nat. Commun. **10**, 5130 (2019).
49. M. Zakharova, S. Reich, A. Mikhaylov, *et al.*, "Inverted Hartmann mask for single-shot phase-contrast X-ray imaging of dynamic processes," Opt. Lett. **44**, 2306–2309 (2019).
50. F. De Marco, S. Savatović, R. Smith, *et al.*, "High-speed processing of X-ray wavefront marking data with the Unified Modulated Pattern Analysis (UMPA) model," Opt. Express **31**, 635–650 (2022).
51. C. A. Neldam, T. Lauridsen, A. Rack, *et al.*, "Application of high resolution synchrotron micro-CT radiation in dental implant osseointegration," J. Cranio-Maxillofacial Surg. **43**, 682–687 (2015).
52. L. Azzi, M. El-Alfy, C. Martel, *et al.*, "Gender differences in mouse skin morphology and specific effects of sex steroids and dehydroepiandrosterone," J. Investig. Dermatol. **124**, 22–27 (2005).
53. L. Birnbacher, S. Maurer, K. Scheidt, *et al.*, "Electron density of adipose tissues determined by phase-contrast computed tomography provides a measure for mitochondrial density and fat content," Front. Physiol. **9**, 707 (2018).
54. H. D. Barth, E. A. Zimmermann, E. Schaible, *et al.*, "Characterization of the effects of X-ray irradiation on the hierarchical structure and mechanical properties of human cortical bone," Biomaterials **32**, 8892–8904 (2011).
55. T. E. Johnson and P. S. Hartman, "Radiation effects on life span in *C*," J. Gerontol. **43**, B137–B141 (1988).
56. Y. Y. How and K. S. Morgan, "Quantifying the X-ray dark-field signal in single-grid imaging," Opt. Express **30**, 10899–10918 (2022).

57. M. K. Croughan, Y. Y. How, A. Pennings, *et al.*, "Directional dark-field retrieval with single-grid X-ray imaging," Opt. Express **31**, 11578–11597 (2023).
58. J. Elliott, G. Davis, and S. Dover, "X-ray microtomography: past and present," Proc. SPIE **7078**, 33–43 (2008).
59. D. John, D. M. Paganin, M.-C. Zdora, *et al.*, "Quantitative stain mapping in X-ray virtual histology," Adv. Sci. e19783 (2026), Early posting.
60. O. Hignette, P. Cloetens, G. Rostaing, *et al.*, "Efficient sub 100 nm focusing of hard X rays," Rev. Sci. Instrum. **76**, 063709 (2005).
61. C. Rau and W. Liu, "Cone-beam imaging with sub-100 nm focal-sized Kirkpatrick–Baez mirrors," Nucl. Instrum. Methods Phys. Res. Sect. A: Accel. Spectrom. Detect. Assoc. Equip. **582**, 132–134 (2007).
62. F. Döring, A.-L. Robisch, C. Eberl, *et al.*, "Sub-5 nm hard X-ray point focusing by a combined Kirkpatrick-Baez mirror and multilayer zone plate," Opt. Express **21**, 19311–19323 (2013).
63. F. Wilde, M. Ogurreck, I. Greving, *et al.*, "Micro-CT at the imaging beamline P05 at PETRA III," AIP Conf. Proc. **1741**, 030035 (2016).
64. M. A. Yakovlev, D. J. Vanselow, M. S. Ngu, *et al.*, "A wide-field micro-computed tomography detector: micron resolution at half-centimetre scale," Synchrotron Radiat. **29**, 505–514 (2022).
65. M. Stampanoni, A. Groso, A. Isenegger, *et al.*, "Trends in synchrotron-based tomographic imaging: the SLS experience," Proc. SPIE **6318**, 193–206 (2006).
66. S. Savatović, F. De Marco, M. Riedel, *et al.*, "Extending the field-of-view of speckle-based microtomography with the UMPA model," Proc. SPIE **13152**, 131520X (2024).
67. S. Savatović, F. De Marco, M. Riedel, *et al.*, "Helical sample-stepping for faster speckle-based multi-modal tomography with the Unified Modulated Pattern Analysis (UMPA) model," J. Instrum. **18**, C11020 (2023).
68. K. Nygård, S. McDonald, J. González, *et al.*, "ForMAX—a beamline for multiscale and multimodal structural characterization of hierarchical materials," Synchrotron Radiat. **31**, 363–377 (2024).
69. S. Flenner, M. Storm, A. Kubec, *et al.*, "Pushing the temporal resolution in absorption and Zernike phase contrast nanotomography: enabling fast in situ experiments," Synchrotron Radiat. **27**, 1339–1346 (2020).
70. T. Weitkamp, D. Haas, D. Wegrzynek, *et al.*, "*ANKAphase*: software for single-distance phase retrieval from inline X-ray phase-contrast radiographs," Synchrotron Radiat. **18**, 617–629 (2011).
71. D. M. Paganin, *Coherent X-Ray Optics, 6* (Oxford University Press, 2006), pp. 400.
72. M. R. Arnison, K. G. Larkin, C. J. Sheppard, *et al.*, "Linear phase imaging using differential interference contrast microscopy," J. Microsc. **214**, 7–12 (2004).
73. C. Kottler, C. David, F. Pfeiffer, *et al.*, "A two-directional approach for grating based differential phase contrast imaging using hard X-rays," Opt. Express **15**, 1175–1181 (2007).
74. D. M. Paganin, *Coherent X-Ray Optics, 6* (Oxford University Press, 2006), pp. 114.
75. E. Pasca, J. S. Jørgensen, E. Papoutsellis, *et al.*, "Core Imaging Library (CIL) (2024).
76. J. S. Jørgensen, E. Ametova, G. Burca, *et al.*, "Core Imaging Library-part I: a versatile Python framework for tomographic imaging," Philos. Trans. Royal Soc. A **379**, 20200192 (2021).
77. W. Van Aarle, W. J. Palenstijn, J. Cant, *et al.*, "Fast and flexible X-ray tomography using the ASTRA toolbox," Opt. Express **24**, 25129–25147 (2016).
78. S. Zandarco, B. Günther, M. Riedel, *et al.*, "Speckle tracking phase-contrast computed tomography at an inverse compton X-ray source," Opt. Express **32**, 28472–28488 (2024).
79. P. Modregger, B. R. Pinzer, T. Thüring, *et al.*, "Sensitivity of X-ray grating interferometry," Opt. Express **19**, 18324–18338 (2011).
80. T. Thüring, P. Modregger, S. Hämmerle, *et al.*, "Sensitivity in X-ray grating interferometry on compact systems," AIP Conf. Proc. **1466**, 293–298 (2012).
81. V. Van Nieuwenhove, J. De Beenhouwer, F. De, *et al.*, "Dynamic intensity normalization using eigen flat fields in X-ray imaging," Opt. Express **23**, 27975–27989 (2015).
82. S. Kalbfleisch, M. Osterhoff, K. Giewekemeyer, *et al.*, "The holography endstation of beamline P10 at PETRA III," AIP Conf. Proc. **1234**, 433–436 (2010).
83. S. Krüger, H. Neubauer, M. Bartels, *et al.*, "Sub-10 nm beam confinement by X-ray waveguides: design, fabrication and characterization of optical properties," Synchrotron Radiat. **19**, 227–236 (2012).
84. S. Savatović, M.-C. Zdora, F. De, *et al.*, "Multi-resolution X-ray phase-contrast and dark-field tomography of human cerebellum with near-field speckles," Biomed. Opt. Express **15**, 142–161 (2023).